

TECHNICAL NOTE • OPEN ACCESS

Controlled growth of transition metal dichalcogenide monolayers using Knudsen-type effusion cells for the precursors

To cite this article: Antony George *et al* 2019 *J. Phys. Mater.* **2** 016001

View the [article online](#) for updates and enhancements.



TECHNICAL NOTE

OPEN ACCESS

RECEIVED

17 August 2018

REVISED

12 December 2018

ACCEPTED FOR PUBLICATION

18 December 2018

PUBLISHED

10 January 2019

Original content from this work may be used under the terms of the [Creative Commons Attribution 3.0 licence](#).

Any further distribution of this work must maintain attribution to the author(s) and the title of the work, journal citation and DOI.



Controlled growth of transition metal dichalcogenide monolayers using Knudsen-type effusion cells for the precursors

Antony George^{1,2,7}, Christof Neumann¹, David Kaiser¹, Rajeshkumar Mupparapu^{2,3}, Tibor Lehnert⁴, Uwe Hübner⁵, Zian Tang¹, Andreas Winter¹, Ute Kaiser⁴, Isabelle Staude^{2,3}  and Andrey Turchanin^{1,2,6,7} 

¹ Friedrich Schiller University Jena, Institute of Physical Chemistry, D-07743 Jena, Germany

² Abbe Centre of Photonics, D-07745 Jena, Germany

³ Friedrich Schiller University Jena, Institute of Applied Physics, D-07745 Jena, Germany

⁴ Ulm University, Central Facility of Materials Science Electron Microscopy, D-89081 Ulm, Germany

⁵ Leibniz Institute of Photonic Technology, D-07745 Jena, Germany

⁶ Jena Center for Soft Matter (JCSM), D-07743 Jena, Germany

⁷ Author to whom any correspondence should be addressed.

E-mail: antony.george@uni-jena.de and andrey.turchanin@uni-jena.de

Keywords: 2D materials, chemical vapor deposition, transition metal dichalcogenides, MoS₂, WS₂

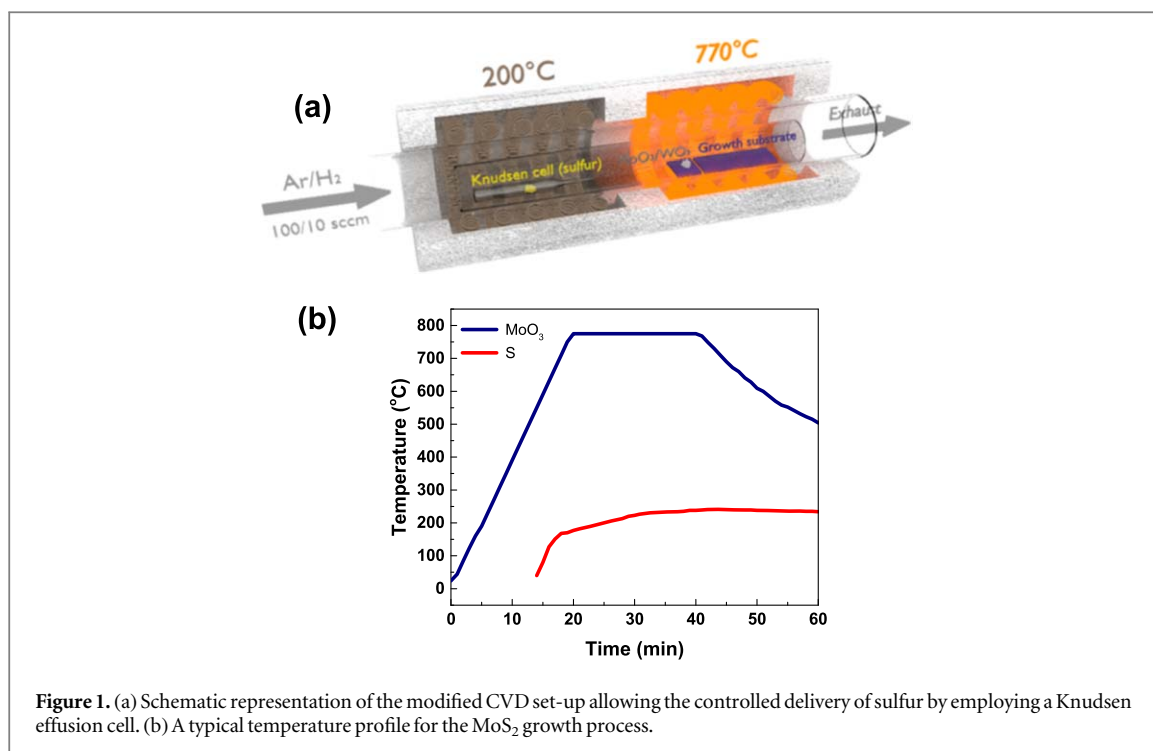
Supplementary material for this article is available [online](#)

Abstract

Controlling the flow rate of precursors is essential for the growth of high quality monolayer single crystals of transition metal dichalcogenides (TMDs) by chemical vapor deposition. Thus, introduction of an excess amount of the precursors affects reproducibility of the growth process and results in the formation of TMD multilayers and other unwanted deposits. Here we present a simple method for controlling the precursor flow rates using the Knudsen-type effusion cells. This method results in a highly reproducible growth of large area and high density TMD monolayers. The size of the grown crystals can be adjusted between 10 and 200 μm . We characterized the grown MoS₂ and WS₂ monolayers by optical, atomic force and transmission electron microscopies as well as by x-ray photoelectron, Raman and photoluminescence spectroscopies, and by electrical transport measurements showing their high optical and electronic quality based on the single crystalline nature.

Introduction

In recent years, semiconducting transition metal dichalcogenides (TMDs) monolayers such as MoS₂, WS₂, WSe₂, MoSe₂, etc have emerged as highly promising materials for ultrathin device technology [1–3]. The unique physical properties of these two-dimensional materials including their optical response [1, 4, 5], electrical field-effect [1, 6, 7], gate induced superconductivity [8], photoluminescence (PL) [9, 10] and valley polarization [11, 12] identify them as candidates for next generation electronic, optoelectronic, sensing and energy conversion devices [1]. For these applications, it is necessary to develop reproducible and economic synthetic routes with a high degree of control over the crystal quality and size. A variety of synthetic approaches have been developed for the growth of TMD monolayers including chemical vapor deposition (CVD) [13–15], physical vapor deposition [16, 17], sulfurization of precursor films [18–21], metal organic chemical vapor deposition [22, 23], etc. Among these approaches, the CVD based synthesis is the most simple and cost effective one for the growth of single crystalline TMD monolayers. In a typical CVD process, powders of metal oxides (e.g. MoO₃, WO₃) and chalcogens (e.g. S, Se) are used as precursors [1, 2]. These precursors are placed inside a reaction tube in open crucibles, heated to appropriate temperatures to be evaporated in a presence of an inert carrier gas transporting them to the target substrate (e.g. SiO₂, sapphire), where they are thermally activated to react and to form the desired TMD monolayers. One of the key parameters for an efficient nucleation and growth of these monolayers are the precursor flow rates in the reaction zone. However, the described above approach provides only a little control over these parameters [1, 2] because the surface area of the precursor powders varies after each loading of the crucibles, which consequently results in different evaporation and flow rates of the materials.



Thus, for chalcogens, which possess a higher vapor pressure in comparison to transition metal oxides, typically a significantly larger amount of the material is provided to a reactor than required for the monolayer growth. The excess chalcogens are then condensed on the colder regions of a CVD reactor. Furthermore, excess supply of the chalcogen precursor results in a reduced crystal size and formation of the multilayer films [24]. In this *technical note*, we present an approach to achieve a higher degree of control over the flow rate of sulfur to the reaction zone of a CVD reactor by using a Knudsen-type effusion cell for this chalcogen precursor instead of an open crucible employed in previous reports. By this simple improvement, we achieve a highly reproducible growth of MoS₂ and WS₂ monolayer single crystals over large surface area on SiO₂ and sapphire substrates. The grown TMD monolayer single crystals have a high surface density and sizes of up to 200 μm . We employ complementary characterization techniques including optical microscopy (OM), atomic force microscopy (AFM), transmission electron microscopy (TEM), x-ray photoelectron spectroscopy (XPS), Raman spectroscopy, PL spectroscopy, and electrical field-effect measurements to study the structural, optical and electronic properties of the grown TMD monolayers. The obtained results clearly demonstrate a good electrical and optical quality of the grown monolayers based on their single crystalline nature.

Experimental

Synthesis of TMDs

MoS₂ growth

Silicon substrates with 300 nm of dry thermal oxide were used as the growth substrate (Sil'tronix, root mean square (rms) roughness <0.2 nm). A schematic representation of the modified CVD setup is shown in figure 1(a). The growth was carried out in a two-zone split tube furnace with a tube diameter of 55 mm (Carbolite Gero). The two-zone configuration allowed us to heat the precursors individually. The substrates were cleaned initially by ultrasonication in acetone for 5 min followed by washing in isopropanol and blowing dry with argon. Within the outer tube, a smaller inner quartz tube of diameter 15 mm was used to place the growth substrates and precursors as shown in figure 1(a). By employing the smaller inner tube the reactants are concentrated to a smaller volume promoting the efficient mixing of precursors. This setup also helps to minimize the amount of precursors required for the growth of TMD monolayers. The quartz Knudsen cell loaded with sulfur powder (99.98%, Sigma Aldrich) was placed in the inner tube and positioned in the center of the first zone of the tube furnace. A detailed description of the Knudsen effusion cell including its dimensions and a photograph are provided in the supporting information (SI) which is available online at stacks.iop.org/JPMATER/2/016001/mmedia, figure S1. Approximately 1–5 μg of MoO₃ powder (99.97%, Sigma Aldrich) were sprinkled on a piece of SiO₂/Si wafer and placed within the inner quartz tube. The MoO₃ precursor and the growth substrates were positioned in the middle of the second zone of the furnace. The growth substrates were

placed next to this at the downstream side. Next, the quartz tube was evacuated to 5×10^{-2} mbar pressure and refilled with argon (5.0, Linde). The growth was carried out at atmospheric pressure under an argon flow of $100 \text{ cm}^3 \text{ min}^{-1}$. The argon gas flow was used to carry the sulfur species to the high temperature reaction area where the MoO_3 precursor and substrates were located. The temperature profile of the MoS_2 growth procedure is shown in figure 1(b). The second zone containing the MoO_3 and the substrates is heated to the growth temperature of $770 \text{ }^\circ\text{C}$ at a rate of $40 \text{ }^\circ\text{C min}^{-1}$ and held at that temperature for 20 min. The temperature of the first zone with sulfur was adjusted to reach $200 \text{ }^\circ\text{C}$ when the second zone reaches $750 \text{ }^\circ\text{C}$. When the temperature of the second zone reached $750 \text{ }^\circ\text{C}$, we introduced hydrogen (5.0, Linde) at a flow rate of $10 \text{ cm}^3 \text{ min}^{-1}$. The hydrogen flow and the furnace were turned off after the growth time of 20 min and the furnace was allowed to cool down to $350 \text{ }^\circ\text{C}$ under an argon flow of $100 \text{ cm}^3 \text{ min}^{-1}$. Then the body of the split furnace was opened to rapidly cool down the sample to room temperature (RT). This procedures result in the growth of mainly monolayer MoS_2 crystals of triangular shape with a typical size ranging from 5 to $200 \text{ }\mu\text{m}$ depending on the position of the substrate from the wafer containing MoO_3 powder.

WS₂ growth

For the growth of WS_2 monolayer crystals, 5 mg of $\text{WO}_{2.9}$ (99.99%, Alfa Aesar) powder mixed with 250 μg of NaCl (99.5%, Carl Roth) were used as precursor. NaCl was used as a growth promoter as previously reported by Eda *et al* [25]. The precursors and growth substrates are positioned inside the growth chamber in a similar manner as explained in the experimental procedure for MoS_2 growth and schematically shown in figure 1(a). In addition to SiO_2/Si wafers we have also tested the growth WS_2 monolayers on c-plane oriented single crystal sapphire substrates (CrysTech GmbH). Then the quartz tube was evacuated to 5×10^{-2} mbar pressure and refilled with argon. The growth was carried out at atmospheric pressure under an argon flow of $100 \text{ cm}^3 \text{ min}^{-1}$. The temperature profile of the WS_2 growth procedure is shown in figure S2. The second zone containing the $\text{WO}_{2.9}$ and the substrates were heated to the growth temperature of $860 \text{ }^\circ\text{C}$ at a rate of $40 \text{ }^\circ\text{C min}^{-1}$ and held at that temperature for 20 min. The sulfur temperature was adjusted to reach $200 \text{ }^\circ\text{C}$ when the second zone reaches $800 \text{ }^\circ\text{C}$. When the temperature of the second zone reached $800 \text{ }^\circ\text{C}$, we introduced H_2 gas at a flow rate of $10 \text{ cm}^3 \text{ min}^{-1}$. The H_2 gas flow and the furnace were turned off after the growth time of 20 min and allowed to cool down to $350 \text{ }^\circ\text{C}$ under an argon flow of $100 \text{ cm}^3 \text{ min}^{-1}$. Then the body of the split furnace was opened to rapidly cool down the sample to RT. This procedures result in the growth of mainly monolayer WS_2 crystals of triangular shape with a typical size ranging from 5 to $70 \text{ }\mu\text{m}$.

Optical microscopy

The OM images were taken with a Zeiss Axio Imager Z1.m microscope equipped with a 5 megapixel CCD camera (AxioCam ICc5) in bright field operation.

Atomic force microscopy

The AFM measurements were performed with an Ntegra (NT-MDT) system in contact mode at ambient conditions using n-doped silicon cantilevers (CSG01, NT-MDT) with a typical tip radius of 6 nm and a typical force constant of 0.03 N m^{-1} .

Transmission electron microscopy

High-resolution TEM measurements were performed using the SALVE (sub-Ångström low-voltage electron microscopy) instrument consisting of a FEI Titan Themis3 column with a CEOS aberration corrector. The corrector is a quadrupole-octupole corrector of modified Rose-Kuhn design that corrects for first order chromatic aberrations, fifth order axial geometric aberrations, and third order off-axial geometric aberrations [26]. The values for the chromatic aberration C_c and the spherical aberration C_s were between -10 and $-20 \text{ }\mu\text{m}$. The electron source is an FEI X-FEG Schottky type and the camera used is an FEI CETA 16M fiber coupled CMOS camera. Images were acquired at an electron accelerating voltage of 60 kV with bright atom contrast using exposure times of 1 s at electron dose rates of about $10^5 \text{ e}^- \text{ nm}^{-2} \text{ s}^{-1}$.

X-ray photoelectron spectroscopy

XPS was performed in a ultra-high vacuum (base pressure 2×10^{-10} mbar) Multiprobe system (Scienta Omicron) using a monochromatized x-ray source (Al $K\alpha$) and an electron analyzer (Argus) with a spectral energy resolution of 0.6 eV. The spectra were calibrated using the $\text{Si}2p$ peak (SiO_2 , 103.6 eV) and fitted using Voigt functions (30:70) after a linear background subtraction.

Raman spectroscopy

The Raman spectra and mapping were acquired using a Bruker Senterra spectrometer operated in backscattering mode. Measurements at 532 nm were obtained with a frequency-doubled Nd:YAG Laser, a 50× objective and a thermoelectrically cooled CCD detector. The spectral resolution of the system is 2–3 cm⁻¹. For all spectra the Si peak at 520.7 cm⁻¹ was used for peak shift calibration of the instrument. The Raman spectroscopy maps were obtained using a motorized XY stage. For analysis of the characteristic MoS₂ and WS₂ peaks the background was subtracted and the data were fitted with Lorentzian functions using a LabVIEW script to determine the peak position, full width at half maximum (FWHM) and maximum intensity of the peaks.

PL spectroscopy

PL from MoS₂ and WS₂ monolayer flakes was characterized with MicroTime 200 laser-scanning confocal fluorescence microscope from PicoQuant GmbH. A pulsed laser of wavelength 532 nm and repetition rate 80 Hz is used to excite the TMD flakes and measure their PL emission with a single-photon avalanche diode detector. A microscope objective of 40× magnification and numerical aperture 0.65 is used to focus the laser onto the flakes, forming a spot of diameter ~1 μm, and to collect the PL emission from the same objective. PL maps were acquired by raster scanning the microscope objective and collecting the PL emission in the spectra range of 650–720 nm using a band pass filter, essentially to collect A-exciton and trion emissions. PL spectra on the TMD flakes were acquired with a spectrometer (Horiba iHR320) coupled with the fiber from the Picoquant confocal microscope setup. Care was taken in all the measurements to block the excitation light reaching the detector using dichroic mirror and notch filter for wavelength 532 nm, in addition to band pass and long pass filters.

Transfer of MoS₂ and WS₂

For device fabrication the MoS₂ and WS₂ crystals were transferred onto Si wafers with 300 nm of SiO₂ (Sil'tronix, rms roughness <0.2 nm) with e-beam lithography (EBL) markers (see below). The transfer step from the growth substrates onto a new Si wafer is essential, as during the growth at elevated temperatures the insulating quality of the SiO₂ layer deteriorates, which results in a significant leakage current by applying a gate voltage. We have employed a poly(methyl methacrylate) (PMMA) assisted transfer protocol for MoS₂ and WS₂ crystals [27]. A PMMA layer of 200 nm (950 kDa, Allresist GmbH, AR-P 679.04) was spin coated onto the SiO₂/Si substrate with CVD grown TMD crystals. Then the substrate was kept floating on top of a bath of KOH (85%, Carl Roth) solution to etch away the SiO₂ layer and to release the TMD crystals supported by PMMA followed by washing several times with ultrapure water (18.2 MΩcm, Membrapure) to remove any residual KOH. Then the PMMA supported MoS₂ was placed on the target substrate and baked at 90 °C for 10 min, followed by immersion in acetone for 2 h to remove the PMMA support and afterwards dried with nitrogen. For preparation of TEM samples the PMMA layer was removed in a critical point dryer (Autosamri 815, Tousimis) to avoid damage of the freestanding areas.

Device fabrication

Heavily p-doped silicon substrates with a thermally grown SiO₂ layer of 300 nm and the transferred TMD monolayers (see above) were processed EBL to fabricate the field-effect transistor (FET) devices. The p-doped silicon base was used as a gate electrode with the 300 nm SiO₂ functioning as a gate dielectric. To define source and drain electrodes a two layer e-beam resist system (AR-P6200 on AR-P617, both from Allresist GmbH Berlin) was spin coated on top of the samples, patterned by EBL (Vistec LION LV1) and subsequently developed (2 min in AR600-546 and 1 min in AR600-50 developer). Then the Au/Ti (50 nm/3 nm) electrodes were deposited by e-beam evaporation process followed by the dissolution of the e-beam resist in AR600-71 overnight.

Electrical measurements

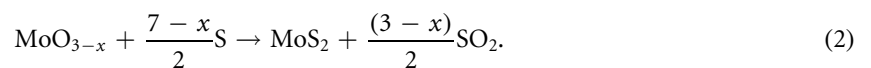
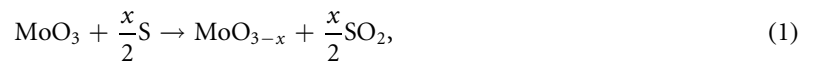
The electrical characterization was carried out with two Keithley 2634B source measure units (SMUs). One SMU was used to change the voltage of the gate with respect to the source/drain in the range between -60 and 60 V for the back-gated devices in vacuum. The other SMU was used to apply the source-drain voltage and measure source-drain current. A Lakeshore vacuum needle probe station TTPX was used to measure the devices in vacuum at a residual pressure about 10⁻⁶ mbar.

Results and discussion

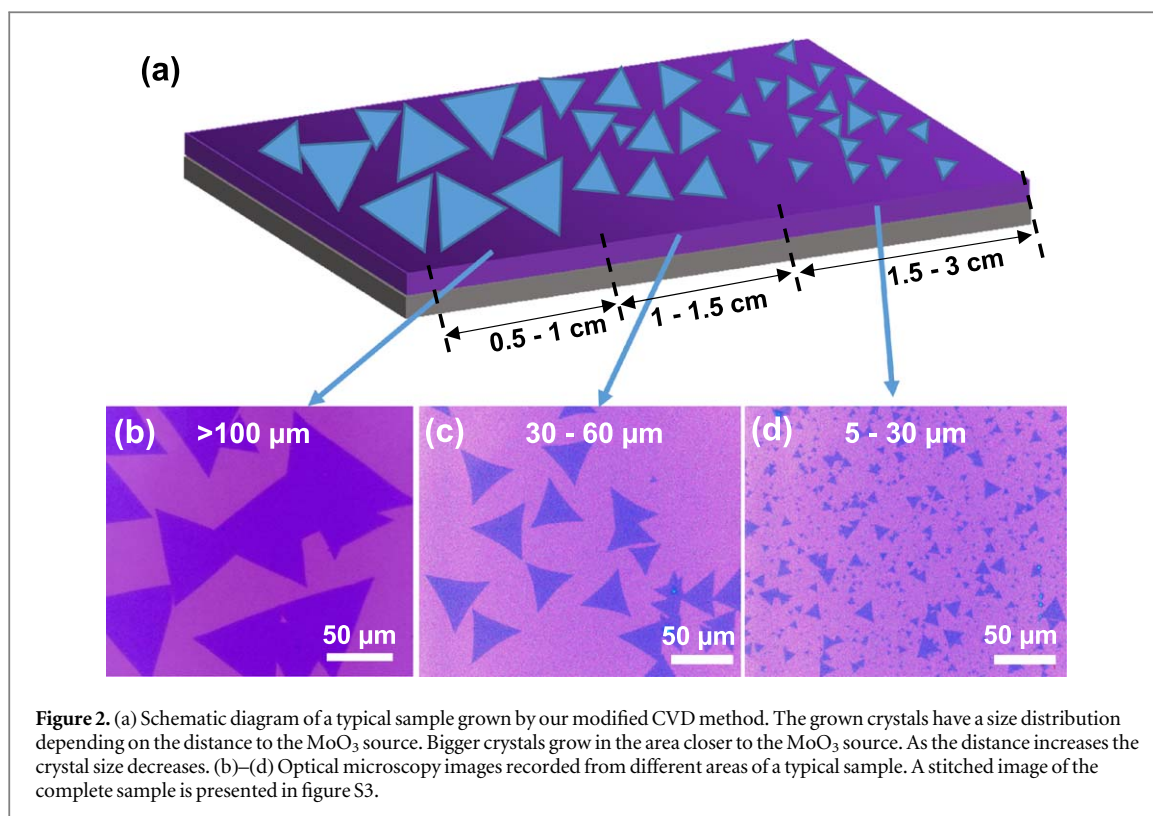
In comparison to previous reports [1, 2], in our CVD setup we mainly employ two modifications. Firstly and most importantly, we use a Knudsen effusion cell to deliver sulfur precursors to the reaction zone in a controllable rate. Secondly, we apply a small inner quartz tube with diameter 15 mm to confine the reaction

process within a small volume promoting proper mixing of the precursors. Note that introduction of a smaller inner tube in CVD growth was reported also previously [28, 29]. Below we describe the modification in more detail. The Knudsen-type evaporation source is a closed container with a small orifice. When the material is heated within the Knudsen cell, it sublimates with a vapor pressure close to the equilibrium one and escapes to the reaction chamber through the orifice. The escaping rate depends on the temperature and the size of the orifice. In our experiments, we have used a reusable quartz container with an orifice diameter of $\sim 85 \mu\text{m}$ as a Knudsen cell for sulfur precursor (see figure S1). The net rate of effusion [30] for Knudsen cells with an infinitely thin orifice is given by $\frac{dn_{\text{eff}}}{dt} = \frac{A(p^{\text{Kcell}} - p^{\text{ch}})}{\sqrt{2\pi MRT}}$, where A is the area of the orifice, p^{Kcell} is the pressure inside the Knudsen cell, p^{ch} is the chamber pressure, M is the molecular mass of the source material, R is the universal gas constant and T is temperature. At $\sim 200^\circ\text{C}$ sulfur has a vapor pressure of ~ 3 mbar [31]. Using these data, we calculated the effusion rate of sulfur atoms as 0.1 mg min^{-1} . In our experiments, we used $\sim 500 \mu\text{g}$ of sulfur for ~ 10 growth cycles of MoS_2 ($\sim 50 \mu\text{g/growth}$). Considering approximately 30–45 min of the sulfur effusion in each growth cycle, the sulfur rate is estimated as $\sim 1\text{--}2 \mu\text{g min}^{-1}$, which is a factor of 100 lower than the theoretical value. This difference is apparently due to a long capillary (~ 2 cm) hosting the orifice of our Knudsen cell (figure S1). In this case the impingement of sulfur species on the capillary walls and their back recoil to the cell has to be considered, which results in a much lower effusion rate of sulfur in comparison to an infinitely thin orifice [32]. Moreover, as the saturated vapor of sulfur consists mainly of a mixture of such species like S_2 , S_3 , S_4 , S_6 , S_7 and S_8 [33], the calculated effusion rate for atomic sulfur is also overestimated due to this reason. In comparison to the conventional TMD growth, where the precursors are placed freely in a reaction tube (see introduction), the amount of evaporated sulfur during a single growth cycle using our Knudsen cell is at least ~ 1000 times lower [24, 34]. Note that H_2S was also reported as a precursor for the growth of good quality large area MoS_2 monolayer films, due to the fact that the flow rate of this gaseous precursor can be precisely controlled using mass flow controllers [35, 36]. However, the maximum lateral sizes of the crystals grown by this method were limited to $10 \mu\text{m}$ [35, 36].

The growth of MoS_2 from solid-state precursors of MoO_3 and S follows the following reaction steps. Initially, a volatile MoO_{3-x} species are generated by the high temperature reduction of the MoO_3 powder [37]. The MoO_{3-x} is transferred to the growth substrate by the carrier gas, adsorbed on the surface and acts as the nucleation sites for MoS_2 crystal growth. The nuclei react with the incoming S forming MoS_2 crystallites. Further MoO_{3-x} absorption takes place at the MoS_2 edges and the growth continues forming single crystal domains. The possible reaction involves the following steps [37]



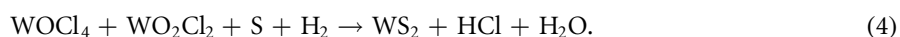
In figure 2(a), we show the schematic of a typical substrate after the growth of MoS_2 crystals. Typically, a substrate with approximate size of $1 \text{ cm} \times 3 \text{ cm}$ was used for the growth. The crystals grow in the form of monolayer triangular domains with a side length ranging from 200 to $5 \mu\text{m}$ depending on the distance to the MoO_3 source. The larger crystals grow in the areas closer to the source and the crystal size decreases as the distance increases. The flux of MoO_{3-x} species is higher in the regions of the substrate located closer to the MoO_3 source, resulting in the growth of large area high-density monolayer crystals. As the distance increases, the flux reduces which results in smaller crystals. In figures 2(b), (c), we show the OM images recorded from three different regions of the growth substrate showing the varying size distribution of the crystals. A stitched optical microscope image of a typical complete sample is presented in figure S3 confirming the large area and high-density growth of MoS_2 crystals by our approach. A quantitative analysis of figure S3 shows that MoS_2 monolayer crystals cover $21\% \pm 1\%$ of the total substrate area, whereas the area with multilayer regions corresponds to $0.6\% \pm 0.1\%$ (see SI for details). We conducted the growth experiments more than 30 times obtaining similar results, which confirms a high reproducibility of the developed method. We also tested the possibility to employ a Knudsen cell for the MoO_3 precursor. These experiments resulted in the growth of smaller monolayer crystals with side lengths in the range of $1\text{--}25 \mu\text{m}$, possibly due to a lower flow of MoO_{3-x} propagating through the opening in comparison to the MoO_3 powder directly places on a substrate (see experimental for details). Despite of the smaller crystal size, this method also yielded a very good reproducibility of the results. It is worth noting that an approach to control the delivery of MoO_3 precursor by employing a predisposed liquid exfoliated/sputtered MoO_3 film on SiO_2/Si substrate as the Mo source in the close proximity of the growth substrate was reported by O'Brien *et al* [38]. Despite this approach resulting in the growth of good quality monolayer MoS_2 films their crystal size was small, which is similar to the results obtained in our experiments where the flow rate of MoO_3 was adjusted by employing a Knudsen effusion cell. We tested the usual method of placing the sulfur powder in an open ceramic crucible for comparison with the improved method using a Knudsen cell. In figures S4(a)–(b) typical samples imaged with an optical microscope are shown. In these particular data and in



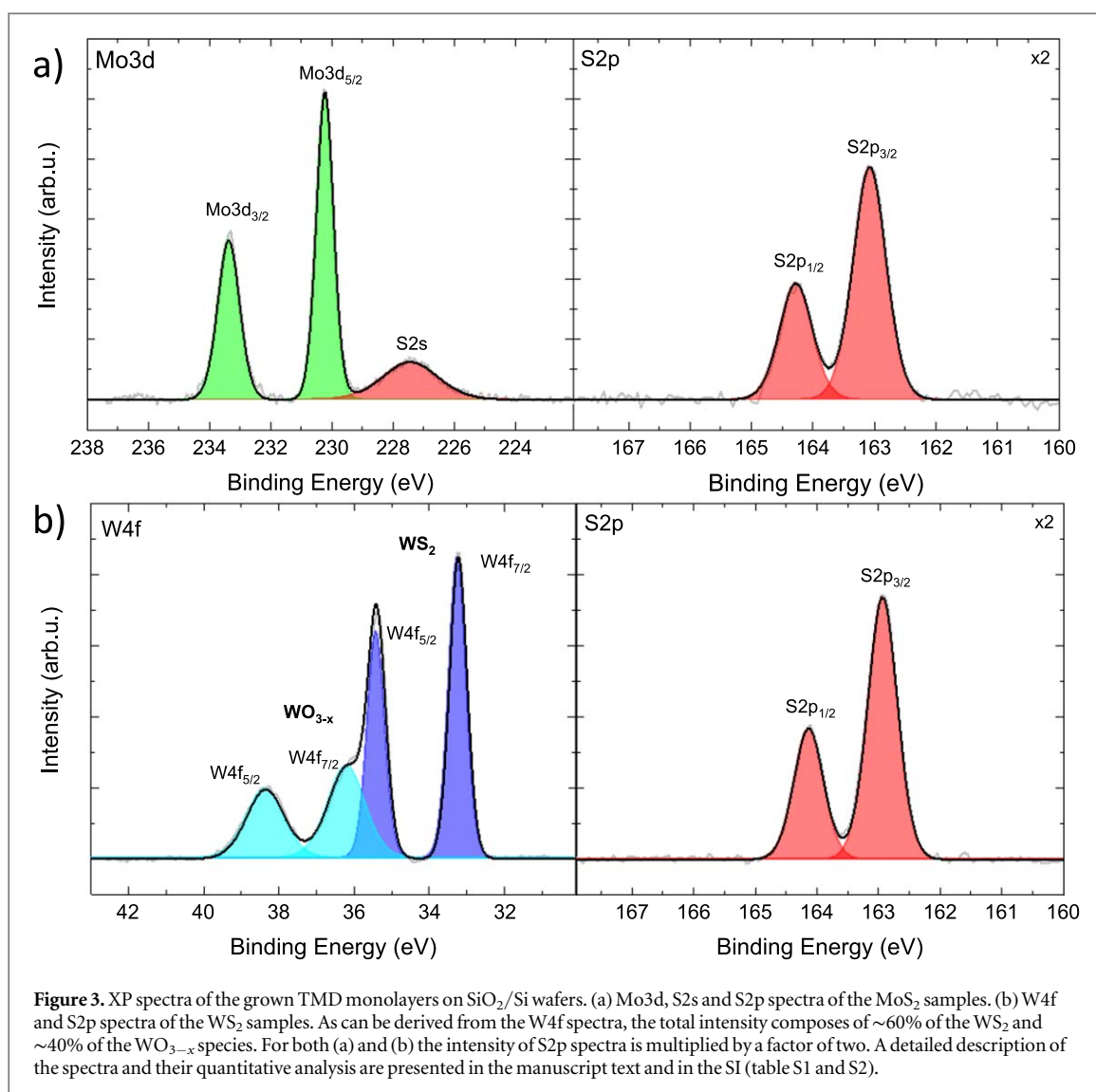
general the following problems are observed: (i) formation of thicker layers and other intermediate compounds along with monolayer crystals, (ii) lower crystal size, (iii) lower reproducibility of the results and (iv) accumulation of excess sulfur at colder regions of the reaction tube. By employing a Knudsen cell in combination with a small inner reaction tube, such problems can be avoided as well as the efficiency and reproducibility of the growth procedure is improved significantly.

We studied the chemical composition of the as grown MoS₂ samples using XPS. Figure 3(a) presents the Mo3d signal showing a single species (green) accompanied by the S2s signal (red) consisting also only of one species, which confirm a high chemical quality and homogeneity of the samples. The binding energy (BE) of the Mo3d_{5/2} signal at 230.2 eV is in a good agreement with the literature data [38]. Similarly, the S2p signal also consists of a single species with a BE of S2p_{3/2} at 163.1 eV. As expected from the spin–orbit coupling, the intensity ratios I(Mo3d_{5/2})/I(Mo3d_{3/2}) and I(S2p_{3/2})/I(S2p_{1/2}) perfectly correspond to 3/2 and 2/1, which additionally confirms that only single species of molybdenum and sulfur are present in the grown monolayers. The elemental ratio of the sulfur to molybdenum was found to be 1.84:1, which corresponds well to the expected ratio of 2:1 within the accuracy of our measurements. The overview spectrum in figure S5(a) reveals only the expected elements: molybdenum, sulfur, oxygen, silicon as well as a small amount of carbon. The latter is due to the airborne carbon contaminations typical for samples transferred at ambient conditions to the UHV system for XPS measurements (figure S5(b)).

For the growth of WS₂ monolayer single crystals, WO_{2.9} (5 mg) mixed with NaCl (250 μg) was used as the source material as reported previously by Eda *et al* [25]. NaCl acts as a growth promoter which helps the quick evaporation of WO_{2.9} by forming a volatile tungsten oxychloride species, which reacts with incoming S to form WS₂ crystals [25]. Typically, a substrate with approximate size of 1 cm × 1 cm was used for the growth of WS₂ crystals. The typical size distribution of the grown crystals are in the range of 5–70 μm. OM images of typical as grown WS₂ crystals grown on SiO₂/Si and c-plane oriented sapphire substrates are presented in figures S6(a), (b) and S6(c), (d), respectively. It is worth noting that the yield and reproducibility of growth experiments were very low without employing NaCl as a growth promoter, possibly due to a low rate of evaporation of WO_{2.9}. The possible chemical reaction resulting in the formation of WS₂ monolayer crystals is given below [25]



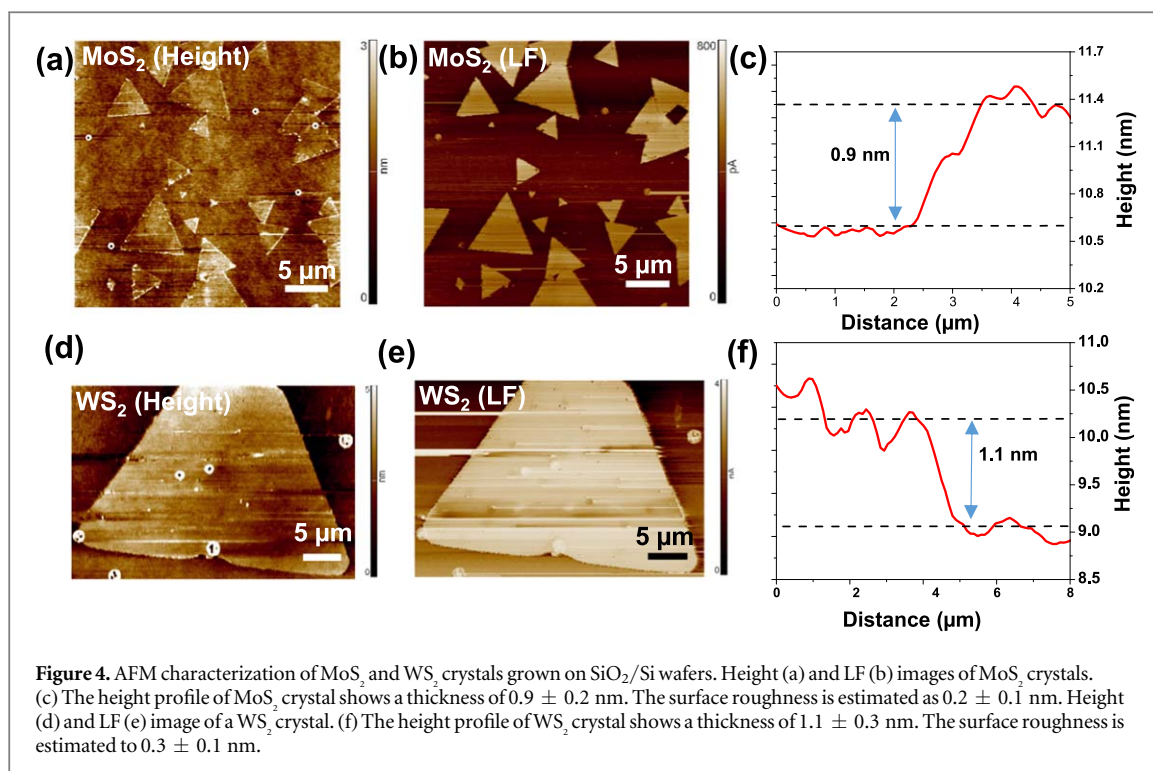
Similar to the grown MoS₂ monolayers, we also analyzed the WS₂ samples using XPS. Figure 3(b) shows the W4f spectrum demonstrating two different tungsten species with the BEs of W4f_{7/2} at 33.2 eV (blue) and 36.2 eV (light blue), respectively [25]. The main component at the BE of 33.2 eV is attributed to the monolayer of WS₂ [25], whereas the second component is assigned to WO_{3-x} [39]. This assignment is confirmed further by



presence of the O1s signal at a BE of 530.3 eV (see figure S7(b)). The intensity ratio of this O1s signal to the W4f_{7/2} signal at 36.2 eV is ~3.6:1, which corresponds well to the stoichiometry of tungsten oxide. The S2p_{3/2} signal shows only a single species with a BE of S2p_{3/2} at 162.9 eV due to the formation of WS₂. An in detail analysis of the intensity ratios of the W4f_{7/2} at 36.2 eV and S2p_{3/2} at 162.9 eV signals as well as the spin-orbit coupling (see SI table S1 and S2) confirms that the samples consist of WS₂ monolayers with some precipitation of WO_{3-x} (see also AFM results below). The overview spectrum of the sample is shown in figure S7(a), which shows that besides the expected components also a small amount of carbon airborne contaminations (similar to MoS₂, see above) as well as sodium (growth promoter, see above) are detected.

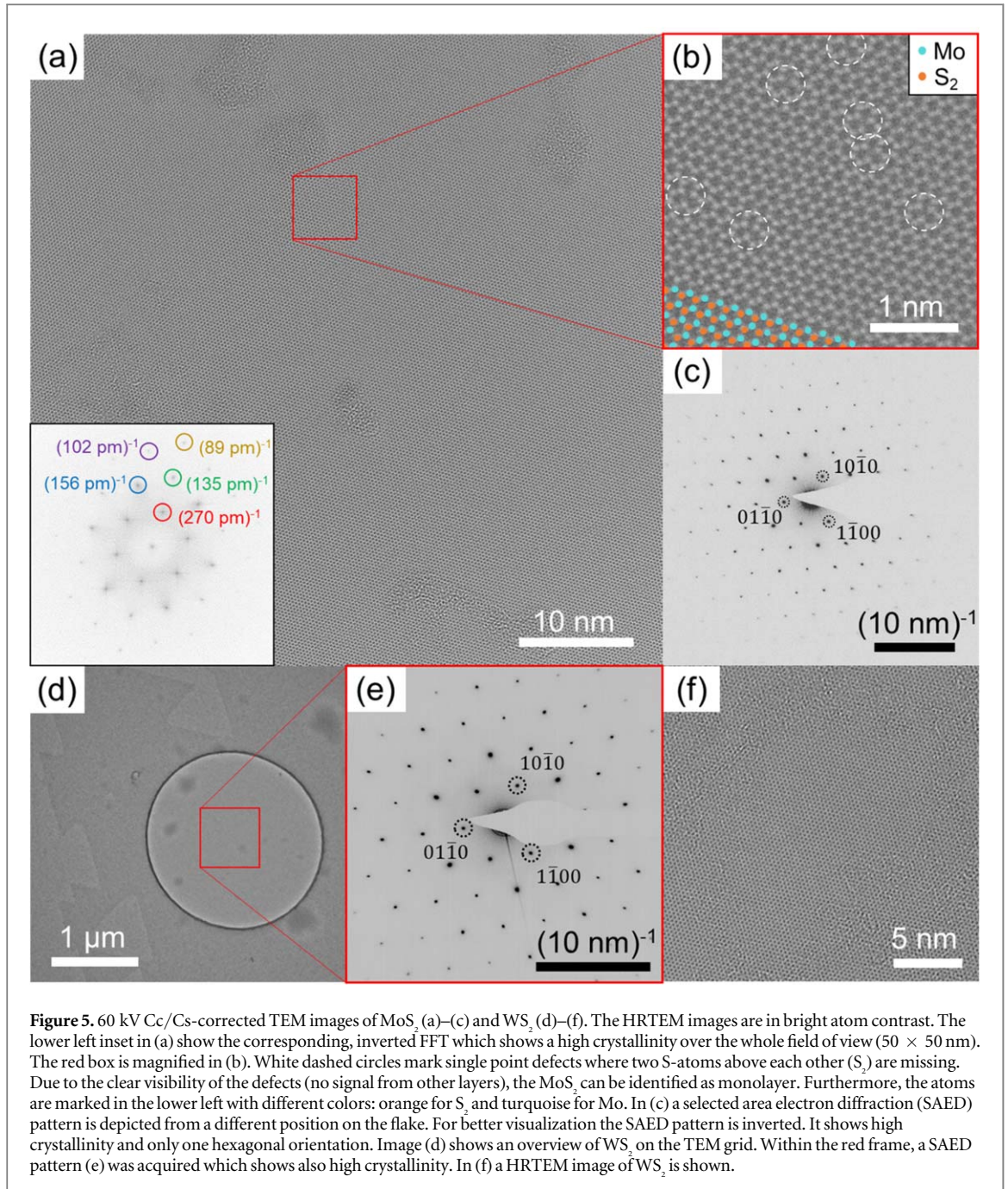
The thickness and surface morphology of the grown crystals were investigated by contact mode AFM height and lateral force (LF) imaging. In figures 4(a) and (b) we present the contact mode AFM topography and LF images recorded on MoS₂ crystals, respectively. A height profile over the edge of a crystal is shown in figure 4(c). The apparent thickness and the rms roughness of the MoS₂ crystals are found to be 0.9 ± 0.2 nm and 0.2 ± 0.1 nm, respectively. In figures 4(d)–(f) we present the respective data for a WS₂ crystal. The thickness of the grown WS₂ crystals is found to be 1.1 ± 0.3 nm and the rms roughness has a value of 0.3 ± 0.1 nm. Some precipitates can be recognized in the AFM images of WS₂ monolayers, which we attribute based on the XPS data to the particles of WO_{3-x}. Both the topography and the LF AFM studies demonstrate a very uniform and flat surface of the grown TMD crystals.

To evaluate the crystallinity and defect structure of the MoS₂ and WS₂ layers on the level of the single atoms and at the same time over a wide field of view, we performed spherical and chromatic aberration-corrected low-voltage TEM and selected area electron diffraction (SAED) [26, 40]. We chose an electron acceleration voltage of 60 kV to reduce the effect of direct collision of the imaging electron with the atomic nucleus [41]. As can be seen from the HRTEM images presented in figure 5, both MoS₂ (a)–(c) and WS₂ (d)–(f) are single crystalline and only point defects were imaged. Figure 5(a) shows MoS₂ in an approximately 50 nm × 50 nm field of view and the



corresponding FFT (inverted) in the left lower inset clearly demonstrating the single-domain hexagonal crystal structure. The red square in (a) is magnified in (b). Here, in the lower left corner, S₂ atoms are colored orange and Mo atoms turquoise. Sulfur point defects, with two missing S atoms above each other (S₂) are marked with white dashed circles; their presence allows unambiguously identifying the film's monolayer nature. From the SAED pattern in (c), as representative for any position chosen on the TEM grid, demonstrates the overall specimen's single-domain crystalline nature. Figures 5(d)–(f) shows very similar high structural quality for the case of the WS₂ layers. The overview image in (d) shows that the WS₂ monolayer covers a much larger area than the ~ 2 μm hole in the TEM grid. Furthermore, triangular-shaped holes in WS₂ are seen. The dark features in the image originate from contamination residuals. The diffraction pattern in (e) obtained from the red square marked area in (d) shows again the single-domain crystalline nature of the material, confirmed by the atomically resolved HRTEM image in (f). It should be noticed that in the case of WS₂ the sulfur point defects were seen occasionally only.

Complementary to AFM and HRTEM, we applied Raman spectroscopy to analyze the structural quality of the grown TMD monolayers. In figure 6(a) we show the Raman spectrum obtained from a MoS₂ crystal on the growth substrate. The spectrum reveals the characteristic peak for a MoS₂ monolayer, which are E' at 384 cm⁻¹ and A'₁ at 405 cm⁻¹ originating from the in-plane vibrations of Mo–S bonds (E'-peak) and out-of-plane vibrations of S atoms (A'₁-peak) [42–45], respectively. The notations E' and A'₁ is used for the monolayer TMDs as suggested by Terrones *et al* to differentiate from the Raman modes of bulk TMDs [44]. A difference between the peak positions (A'₁ - E') is 21 cm⁻¹ confirming that the MoS₂ crystals are monolayers [38]. The FWHM of the E'-peak is found to have a narrow value of 4.5 cm⁻¹ indicating a good crystallinity of the grown MoS₂ crystals without the presence of the amorphous phase [43]. A map of the E'- and A'₁-peak intensities recorded on MoS₂ crystals are shown in figure 6(b) and figure S8 respectively. The Raman maps reveal a uniform intensity distribution in the entire area of grown crystals indicating a good crystallinity. In figure 6(c), we show the Raman spectrum obtained from a WS₂ crystal on the growth substrate. The spectrum reveals the characteristic first-order and second-order peaks such as LA(M) at 176 cm⁻¹ (longitudinal acoustic mode), E' at 356 cm⁻¹, A'₁ at 419 cm⁻¹ and 2LA(M) at 352 cm⁻¹ [43, 44, 46]. The LA(M) and 2LA(M) peaks are originating from the longitudinal acoustic phonons, which are in-plane collective periodic compressions and expansions of atoms in the lattice. For monolayer WS₂ crystals, the second order 2LA(M) peak shows a very strong intensity when using an excitation wavelength of 532 nm [43, 46]. The E'- and A'₁-peaks are originating from the in-plane vibrations of W–S bonds and out-of-plane vibration of S atoms in the WS₂ lattice, respectively. A map of the 2LA(M) and A'₁-peak intensities are shown in figure 6(d) and figure S9, respectively. Similar to MoS₂, the Raman maps reveal a uniform intensity distribution in the entire area of the grown WS₂ crystals indicating their uniform structural quality. In table S3 and S4, we present a statistical analysis of the Raman data obtained from the maps.



The optical quality of the grown TMD crystals was further analyzed using PL spectroscopy and imaging. A PL spectrum obtained on a MoS₂ crystal, figure 6(e), reveals the excitonic transition peaks corresponding to A-exciton at 681 nm, and B-exciton at 626 nm, which are in agreement with the literature data [47]. Similarly, a PL spectrum obtained on a WS₂ crystal, figure 6(g), displays the excitonic peak at 643 nm [9]. A smaller peak at 665 nm is seen as a shoulder of the A-exciton peak is due to trion excitation [48]. The PL maps obtained from both MoS₂ and WS₂ crystals are presented in figures 6(f) and (h), respectively. The maps show a very uniform intensity of the PL emission throughout the crystals area demonstrating their good optical quality.

The electronic performance of the CVD grown TMD monolayers was tested by their implementation in FET devices. In figure 7(a) a typical transfer curve (the enhancement in drain current with applied gate voltage) of a MoS₂ FET is shown. From the transfer characteristics, we have estimated the field effect mobility using

$$\mu = \left(\frac{dI_{ds}}{dV_{bg}} \right) \left(\frac{L}{WC_{ox}V_{ds}} \right),$$

where L is the channel length, W is the channel width, C_{ox} is the capacitance of the 300 nm gate oxide and V_{ds} is the source–drain voltage. The device shows a mobility of $5.4 \text{ cm}^2 \text{ V}^{-1} \text{ s}^{-1}$ and an on–off ratio in the order of 10^7 . The inset of figure 7(a) shows an OM image of MoS₂ devices. The average mobility value obtained from 8 devices is $4.0 \pm 1.1 \text{ cm}^2 \text{ V}^{-1} \text{ s}^{-1}$. In figure 7(b), a typical transfer curve of a WS₂

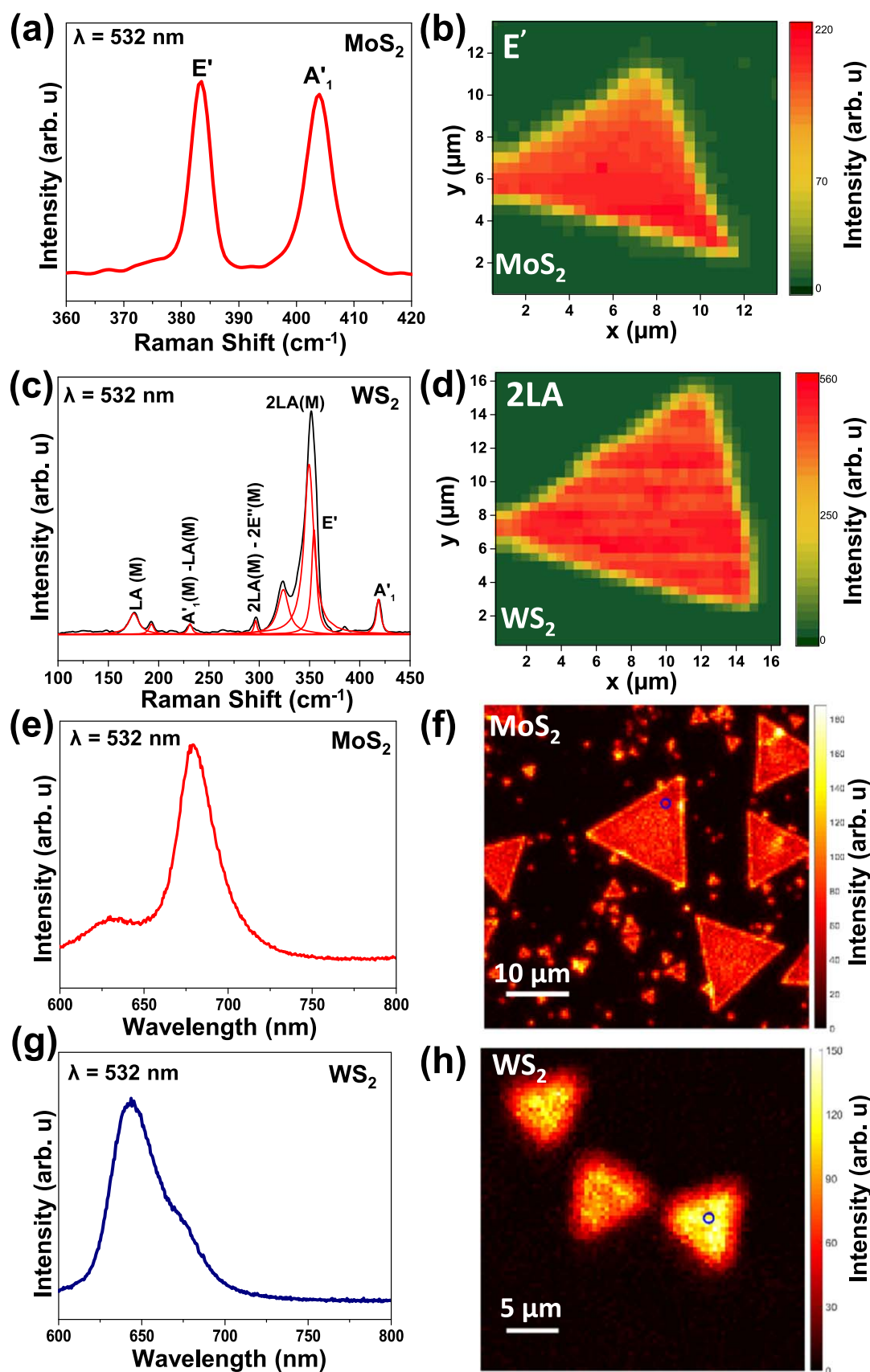
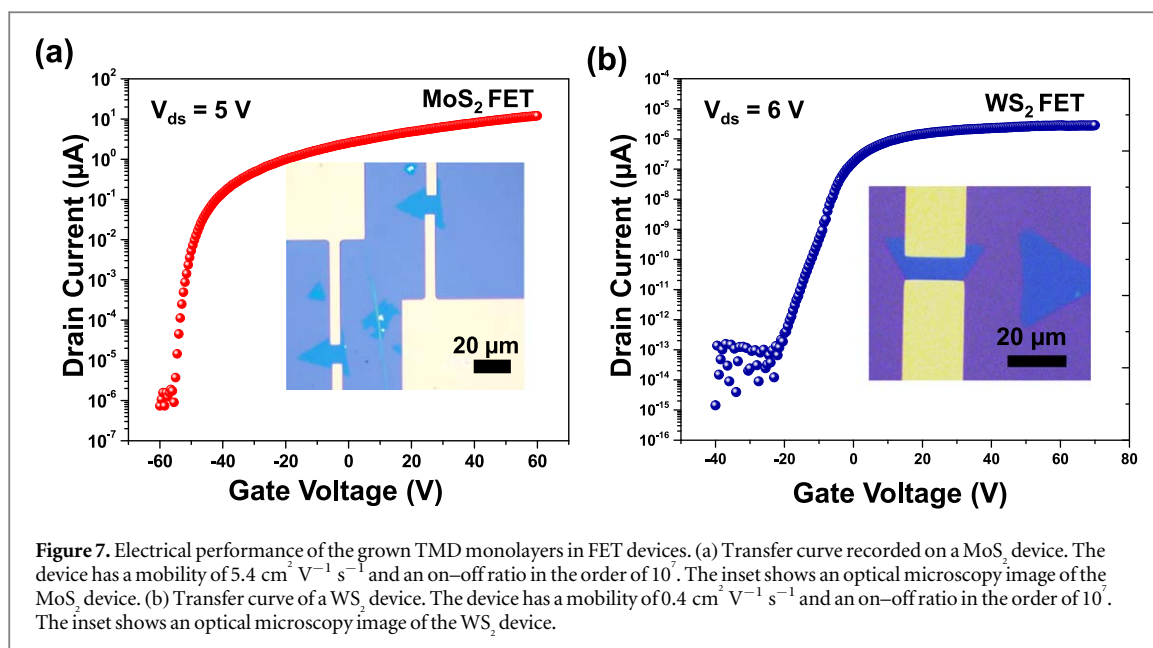


Figure 6. Raman and photoluminescence (PL) spectroscopy characterization of the MoS₂ and WS₂ monolayer crystals grown on SiO₂. (a) A Raman spectrum of MoS₂. (b) The intensity map of E' band of MoS₂. The map shows a uniform intensity distribution indicating a uniform structural quality of the crystal. An intensity map of the A'₁ band is presented in figure S8. (c) A Raman spectrum of WS₂. (d) An intensity map of the 2LA band shows a uniform intensity distribution and therefore a uniform structural quality. An intensity map of the A'₁ band of WS₂ is presented in figure S9. (e) PL emission spectrum recorded from a monolayer of MoS₂. (f) A PL intensity map of MoS₂ crystals showing a uniform emission. (g) A PL emission spectrum recorded from a monolayer WS₂.



FET is shown. The device shows a mobility of 0.4 cm² V⁻¹ s⁻¹ and an on–off ratio in the order of 10⁷. The average mobility value estimated from 8 devices is 0.2 ± 0.1. The mobility and on–off ratios are in the range of typical values reported for devices made of CVD grown samples on SiO₂/Si substrate [49–51] showing the applicability of the grown crystals for electronic and optoelectronic devices. Despite a lower density of the point defects in the grown WS₂ in comparison to MoS₂, as shown by HRTEM (see figure 5), the field effect mobility in WS₂ is lower than MoS₂ suggesting that this difference is due to the intrinsic electronic properties of both materials on SiO₂ substrate in back-gated device configuration. Furthermore, the mobility of TMD monolayer crystals greatly depends on the substrate and encapsulation, and therefore may be improved by, e.g. fabricating encapsulated devices in the top-gated configuration as shown by Duesberg *et al* [52].

Summary

We have demonstrated a modified approach for the CVD growth of MoS₂ and WS₂ monolayers by employing Knudsen effusion cells for the sulfur precursor. Because of a better control over the flow rate of sulfur to the reaction zone, our approach results in a reproducible growth of large area and high density single crystals of the TMD monolayers. The size of the grown crystals is in the range of 10–200 µm, which is adjusted by a distance between the growth substrate and the transition metal source. Our complementary microscopic, spectroscopic, photonic and electrical transport characterization shows that the grown MoS₂ and WS₂ monolayers possess high structural, chemical, electronic and optical quality enabling their implementation in electronic, photonic and optoelectronic devices. We expect that the use of Knudsen cells for solid-state precursors can significantly improve also the growth of other TMD monolayers such as WSe₂, MoSe₂, TaS₂, NbSe₂, etc.

Acknowledgments

We acknowledge financial support of the Thüringer MWWDG via the ‘ProExzellenz 2014–2019’ programme under the grants ‘ACP^{Explore}2016’ and ‘ACP^{Explore}2018’ as well as the Deutsche Forschungsgemeinschaft (DFG) through a research infrastructure grant INST 275/257-1 FUGG. This project has also received funding from the joint European Union’s Horizon 2020 and DFG research and innovation programme FLAG-ERA under a grant TU149/9-1. TL and UK acknowledge funding from the German Research Foundation (DFG) and the Ministry of Science, Research and the Arts (MWK) of the federal state of Baden-Württemberg (Germany) in the frame of the SALVE project (www.salve-project.de) as well as the European Union in the frame of the Graphene Flagship. We thank Stephanie Höppener and Ulrich S Schubert for enabling our Raman spectroscopy and microscopy studies at the JCSM.

ORCID iDs

Isabelle Staudé  <https://orcid.org/0000-0001-8021-572X>

Andrey Turchanin  <https://orcid.org/0000-0003-2388-1042>

References

- [1] Choi W, Choudhary N, Han G H, Park J, Akinwande D and Lee Y H 2017 *Mater. Today* **20** 116–30
- [2] Cai Z, Liu B, Zou X and Cheng H M 2018 *Chem. Rev.* **118** 6091–133
- [3] Manzeli S, Ovchinnikov D, Pasquier D, Yazyev O V and Kis A 2017 *Nat. Rev. Mater.* **2** 17033
- [4] Tan H, Fan Y, Zhou Y, Chen Q, Xu W and Warner J H 2016 *ACS Nano* **10** 7866–73
- [5] Ying X et al 2017 *Adv. Mater.* **29** 1605972
- [6] Ovchinnikov D, Allain A, Huang Y-S, Dumcenco D and Kis A 2014 *ACS Nano* **8** 8174–81
- [7] Xu Z-Q et al 2015 *ACS Nano* **9** 6178–87
- [8] Ye J T, Zhang Y J, Akashi R, Bahramy M S, Arita R and Iwasa Y 2012 *Science* **338** 1193–6
- [9] Gutiérrez H R, Perea-López N, Elías A L, Berkdemir A, Wang B, Lv R, López-Urías F, Crespi V H, Terrones H and Terrones M 2013 *Nano Lett.* **13** 3447–54
- [10] Sun L, Zhang X, Liu F, Shen Y, Fan X, Zheng S, Thong J T L, Liu Z, Yang S A and Yang H Y 2017 *Sci. Rep.* **7** 16714
- [11] Mak K F, He K, Shan J and Heinz T F 2012 *Nat. Nanotechnol.* **7** 494
- [12] Nayak P K, Lin F-C, Yeh C-H, Huang J-S and Chiu P-W 2016 *Nanoscale* **8** 6035–42
- [13] Najmaei S, Liu Z, Zhou W, Zou X, Shi G, Lei S, Yakobson B I, Idrobo J-C, Ajayan P M and Lou J 2013 *Nat. Mater.* **12** 754
- [14] van der Zande A M, Huang P Y, Chenet D A, Berkelbach T C, You Y, Lee G-H, Heinz T F, Reichman D R, Muller D A and Hone J C 2013 *Nat. Mater.* **12** 554
- [15] Chunxiao C, Jingzhi S, Xing W, Bingchen C, Namphung P, Caiyu Q, Litao S and Ting Y 2014 *Adv. Opt. Mater.* **2** 131–6
- [16] Muratore C, Hu J J, Wang B, Haque M A, Bultman J E, Jespersen M L, Shamberger P J, McConney M E, Naguy R D and Voevodin A A 2014 *Appl. Phys. Lett.* **104** 261604
- [17] Gong C et al 2013 *ACS Nano* **7** 11350–7
- [18] Payam T et al 2016 *Mater. Res. Express* **3** 075009
- [19] Lin Y-C, Zhang W, Huang J-K, Liu K-K, Lee Y-H, Liang C-T, Chu C-W and Li L-J 2012 *Nanoscale* **4** 6637–41
- [20] John R, Xue L, Chunlei Y, Matthew E and Jiang W 2017 *2D Mater.* **4** 045007
- [21] Lee K, Gatensby R, McEvoy N, Hallam T and Duesberg G S 2013 *Adv. Mater.* **25** 6699–702
- [22] TaeWan K, Jihun M, Hyeji P, DaeHwa J, Mangesh D, Chegal W, Jonghoo P, Soo-Hwan J and Sang-Woo K 2017 *Nanotechnology* **28** 18LT01
- [23] Kang K, Xie S, Huang L, Han Y, Huang P Y, Mak K F, Kim C-J, Muller D and Park J 2015 *Nature* **520** 656
- [24] Chen B, Yu Q, Yang Q, Bao P, Zhang W, Lou L, Zhu W and Wang G 2016 *RSC Adv.* **6** 50306–14
- [25] Li S, Wang S, Tang D-M, Zhao W, Xu H, Chu L, Bando Y, Golberg D and Eda G 2015 *Appl. Mater. Today* **1** 60–6
- [26] Linck M et al 2016 *Phys. Rev. Lett.* **117** 076101
- [27] Turchanin A, Beyer A, Nottbohm C T, Zhang X, Stosch R, Sologubenko A, Mayer J, Hinze P, Weimann T and Götzhäuser A 2009 *Adv. Mater.* **21** 1233–7
- [28] Wang C et al 2014 *Sci. Rep.* **4** 4537
- [29] Cong C, Shang J, Wu X, Cao B, Peimyo N, Qiu C, Sun L and Yu T 2014 *Adv. Opt. Mater.* **2** 131–6
- [30] Swan T H and Mack E 1925 *J. Am. Chem. Soc.* **47** 2112–6
- [31] West W A and Menzies A W C 1928 *J. Phys. Chem.* **33** 1880–92
- [32] Clausen P 1932 *Ann. Phys.* **406** 134–8
- [33] Berkowitz J and Marquart J R 1963 *J. Chem. Phys.* **39** 275–83
- [34] Zhou D, Shu H, Hu C, Jiang L, Liang P and Chen X 2018 *Cryst. Growth. Des.* **18** 1012–9
- [35] Dumitru D, Dmitry O, Oriol Lopez S, Philippe G, Duncan T L A, Sorin L, Aleksandra R and Andras K 2015 *2D Mater.* **2** 044005
- [36] Youngchan K, Hunyoung B, Gyeong Hee R, Zonghoon L and Changgu L 2016 *J. Phys.: Condens. Matter* **28** 184002
- [37] Lin L X and Dong L Y 2003 *Chem. Eur. J.* **9** 2726–31
- [38] O'Brien M, McEvoy N, Hallam T, Kim H-Y, Berner N C, Hanlon D, Lee K, Coleman J N and Duesberg G S 2014 *Sci. Rep.* **4** 7374
- [39] Bittencourt C, Felten A, Mirabella F, Ivanov P, Llobet E, Silva M A P, Nunes L A O and Pireaux J J 2005 *J. Phys.: Condens. Matter* **17** 6813
- [40] Kaiser U et al 2011 *Ultramicroscopy* **111** 1239–46
- [41] Komsa H-P, Kotakoski J, Kurasch S, Lehtinen O, Kaiser U and Krasheninnikov A V 2012 *Phys. Rev. Lett.* **109** 035503
- [42] Lee C, Yan H, Brus L E, Heinz T F, Hone J and Ryu S 2010 *ACS Nano* **4** 2695–700
- [43] Zhang X, Qiao X-F, Shi W, Wu J-B, Jiang D-S and Tan P-H 2015 *Chem. Soc. Rev.* **44** 2757–85
- [44] Terrones H et al 2014 *Sci. Rep.* **4** 4215
- [45] Saito R, Tatsumi Y, Huang S, Ling X and Dresselhaus M S 2016 *J. Phys.: Condens. Matter* **28** 353002
- [46] Berkdemir A et al 2013 *Sci. Rep.* **3** 1755
- [47] Splendiani A, Sun L, Zhang Y, Li T, Kim J, Chim C-Y, Galli G and Wang F 2010 *Nano Lett.* **10** 1271–5
- [48] Wei K, Liu Y, Yang H, Cheng X and Jiang T 2016 *Appl. Opt.* **55** 6251–5
- [49] Najmaei S et al 2014 *Nano Lett.* **14** 1354–61
- [50] Schmidt H et al 2014 *Nano Lett.* **14** 1909–13
- [51] Lan C, Li C, Yin Y and Liu Y 2015 *Nanoscale* **7** 5974–80
- [52] Kim H, Kim W, O'Brien M, McEvoy N, Yim C, Marcia M, Hauke F, Hirsch A, Kim G-T and Duesberg G S 2018 *Nanoscale* **10** 17557–66